

Subgrid-scale modeling sensitivities in wall-modeled large-eddy simulations of a high-lift aircraft configuration

By K. Goc, S. T. Bose[†] AND P. Moin

1. Motivation and objectives

This research brief describes follow-on work to our earlier study (Goc *et al.* 2019, 2020), where we used wall-modeled large-eddy simulation (WMLES) to simulate a realistic aircraft configuration across the lift curve. We describe herein subgrid-scale (SGS) modeling sensitivities on two grids, one numbering 10 million control volumes (McV) and another numbering 42 McV. Two eddy-viscosity-based SGS modeling approaches are considered, the static coefficient Vreman model (Vreman 2004) and the dynamic coefficient Smagorinsky model (Germano *et al.* 1991). In addition to exploration of SGS modeling sensitivities, we build upon earlier work (Goc *et al.* 2019) by including the nacelle/pylon installation and simulating the wind tunnel test section. We consider this geometry to be the highest-fidelity representation of the JAXA experimental test campaign (Yokokawa *et al.* 2008) that is available to the public, since the geometry of the contraction/expansion sections of the low-speed wind tunnel explored by Ito *et al.* (2019) is not open-source.

2. Background: solver and modeling approach

The second-order low-dissipation finite-volume solver charLES (Ham *et al.* 2006) is leveraged for the present study. The wall-model/LES interface is at the first cell centroid. No time filtering of the LES signal (*à la* Yang *et al.* 2017) is applied because limited sensitivity to these choices has been observed in unpublished studies at the Center for Turbulence Research, in particular in the context of channel flows using hexagonal close-packed (HCP) grids, which are the same as those used in the present simulations. A stress-based wall-modeling approach is employed in these simulations, in which unsteady LES content at the wall-model/LES exchange location is used to supply a boundary condition to the wall model, whose role is to provide a wall stress that acts on the outer LES solution through a Neumann boundary condition. An algebraic formulation of the wall-model equations, which assume a turbulent boundary layer in equilibrium (as in Kawai & Larsson 2012), are solved at each wall-adjacent cell centroid at each time step through a non-linear root finding algorithm in the calculations described herein. The model formulation is shown in Goc *et al.* (2019). A thorough discussion of stress-based wall modeling approaches is presented by Bose & Park (2018).

3. Numerical setup

The simulated geometry is the JAXA standard model, which was the focus of the Third AIAA High-Lift Prediction Workshop, with results and conclusions detailed by

[†] Cascade Technologies Inc., Palo Alto.

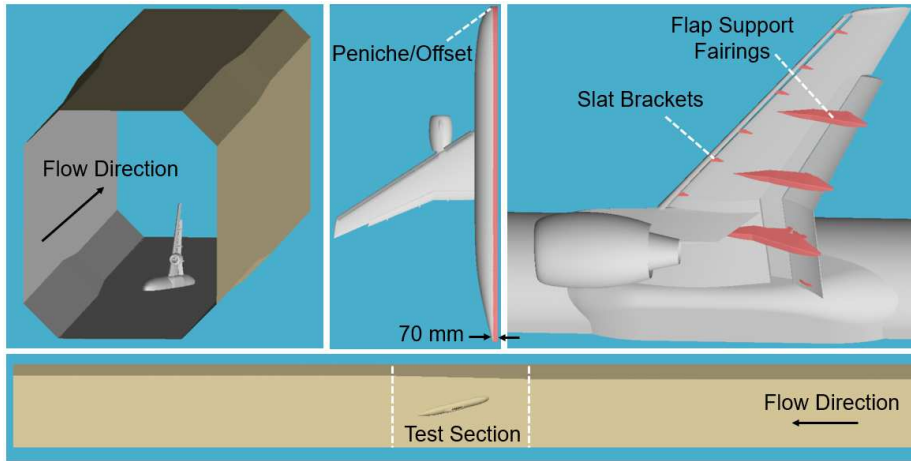


FIGURE 1. Computer-aided design model of the JAXA standard model in the JAXA low-speed wind tunnel, including octagonal test section, sidewall mounting peniche/offset, and nacelle/pylon installation.

Rumsey *et al.* (2018). The geometry of the wind tunnel experiment is reproduced to a high degree of detail with the octagonal test section and peniche/offset sidewall mounting system included in the computer-aided design model, which is shown in Figure 1. The aircraft includes the bracketry associated with deployed high-lift devices as well as a flow-through (passive) nacelle about a third of the span along the wing. The nacelle does not have a chine.

Regarding the boundary conditions, we have prescribed a uniform plug flow at the inlet which matches the test conditions of Yokokawa *et al.* (2008). A viscous wall-modeled boundary condition is applied on the wind tunnel walls, with a δ_{99} value that is within 10 mm of the value of 140 mm quoted by Ito *et al.* (2019). At the outflow, we have prescribed a characteristic non-reflecting boundary condition, in which we prescribe a freestream outlet pressure. The boundary condition is based on the approach developed by Poinsot & Lele (1992).

Slices of the grid are shown in Figures 2 and 3. The grids are generated by computing a Voronoi diagram of the water tight volume around the aircraft as in Du *et al.* (2006), using a staggered point seeding, which results in the HCP topology shown in the figures. The cells are locally isotropic, and refinement windows are set based on the distance to the nearest boundary. This topology is conducive to low numerical dissipation calculations as cell faces always perpendicularly bisect the line connecting adjacent control volumes. The 42 Mcv grid is obtained from the 10 Mcv grid by adding a layer of twofold refined isotropic HCP cells adjacent to the solid boundary of the domain, accounting for the additional 32 Mcv in the finer grid. An *a posteriori* estimate of the number of points per trailing-edge boundary-layer thickness on the inboard part of the wing revealed $\delta/\Delta \approx 10$ on the 10 Mcv grid and $\delta/\Delta \approx 20$ on the 42 Mcv grid, with δ the local boundary-layer thickness and Δ the local cell length scale. In viscous units, the first cell achieved a maximum $y^+ \approx 320$ on the 10 Mcv grid and a maximum $y^+ \approx 160$ on the 42 Mcv grid at the wing leading edge.

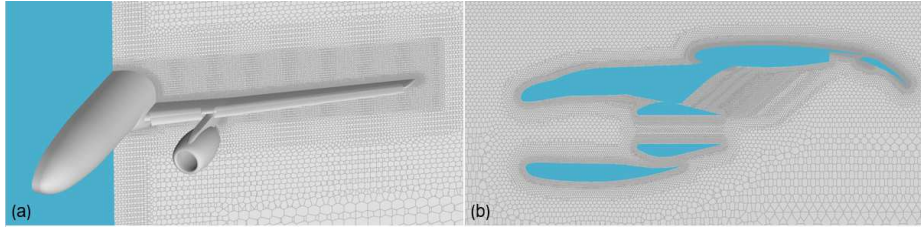


FIGURE 2. Slices of the hexagonal close-packed grid from the 42 Mcv grid along the span of the wing (a) and through the nacelle/pylon region (b). A refinement box around the wing adds grid support for off-body flow features such as viscous wakes and shear layers.

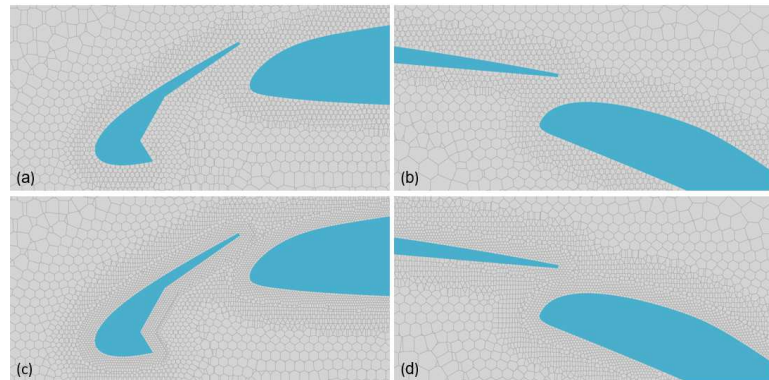


FIGURE 3. Slices of the hexagonal close-packed grid near the slat (a,c) and flap (b,d) for the 10 Mcv (a,b) and 42 Mcv (c,d) grids. The grids differ in that the finer grid contains a layer of refinement in the wall-adjacent viscous region.

4. Results: 42 Mcv grid

We begin our discussion of the results using the 42 Mcv grid, which was built so as to fit $\delta_{chord}/\Delta \approx 10$, with δ_{chord} being the boundary-layer thickness based on the mean aerodynamic chord, estimated using a flat-plate turbulent correlation for the boundary-layer thickness. This estimate proved to be conservative, as mentioned before, as the output of the calculation revealed $\delta_{chord}/\Delta \approx 20$ at the trailing edge on the inboard part of the wing.

Exploration of SGS modeling sensitivities, which is the focus of this brief, was motivated by the inadequate (>5 lift counts of error) prediction of lift in both the linear and near-stall regime by the Vreman SGS model on the 42 Mcv grid. The dynamic Smagorinsky model (DSM) (Germano *et al.* 1991) with the modification by Lilly (1992) was evaluated because its model coefficient is set using a dynamic procedure that leverages information in the resolved scales to adjust the model coefficient in time and space. In contrast, the static Vreman model uses a coefficient obtained via calibration to homogeneous isotropic turbulence (Vreman 2004). We hypothesized that the dynamic procedure would result in greater predictive capability of the SGS model. Indeed, we find that in both the linear region of the lift curve shown in Figure 4 and the near-stall region, DSM systematically outperforms Vreman on the 42 Mcv grid. The same improvement holds when considering drag coefficient (Figure 5), while improvement in pitching moment (Figure 6) is not readily discernible.

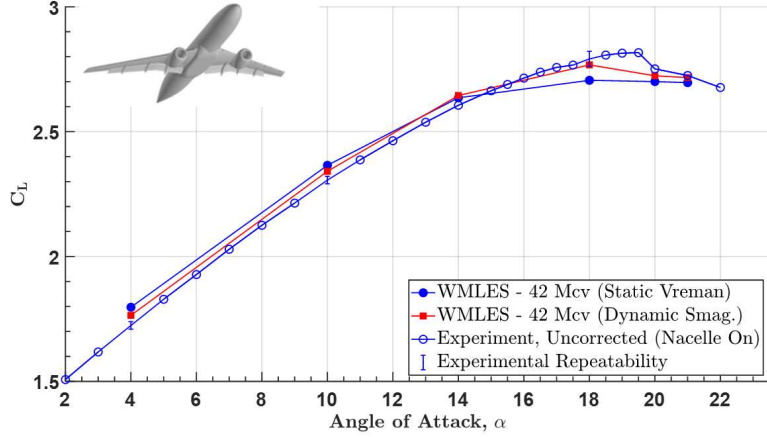


FIGURE 4. Lift coefficient (C_L) plotted against aircraft angle of attack (α) in degrees for the JAXA standard model (nacelle/pylon on configuration) as compared with the predictions of charLES using two SGS modeling approaches: static Vreman and dynamic Smagorinsky. Uncorrected experimental data is plotted for comparison against charLES results that include the wind tunnel test section and peniche geometry.

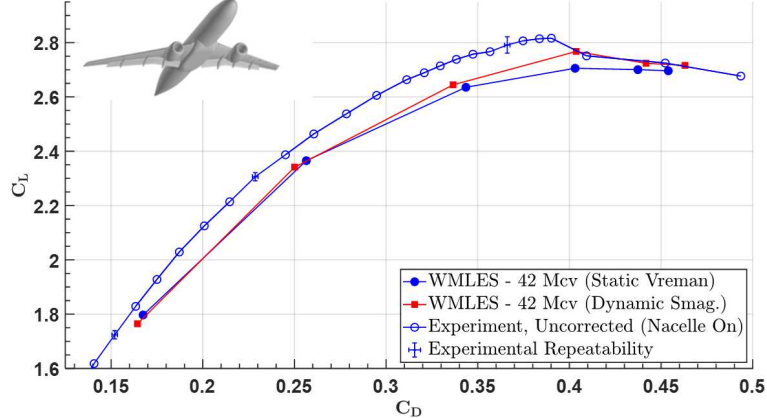


FIGURE 5. Drag polar (C_L vs. C_D) of the JAXA standard model (nacelle/pylon on configuration) as compared with the predictions of charLES using two SGS modeling approaches: static Vreman and dynamic Smagorinsky.

4.1. Breakdown of force contributions by component

In the next subsections, we aim to identify the regions in the flow field where the DSM model outperforms the static Vreman model. To that end, we use Figure 7, in which we have reported the total lift force, as well as the contribution of various parts of the aircraft to the aggregate total. As expected, the main element of the wing contributes the most to the total lift coefficient, C_L .

4.1.1. Linear region of the lift curve

Upon further investigation of the contributions to the lift coefficient shown in Figure 7, we find that in the linear regime, the lift overprediction achieved with the static coefficient Vreman model is ameliorated by DSM due to the prediction of less lift on the

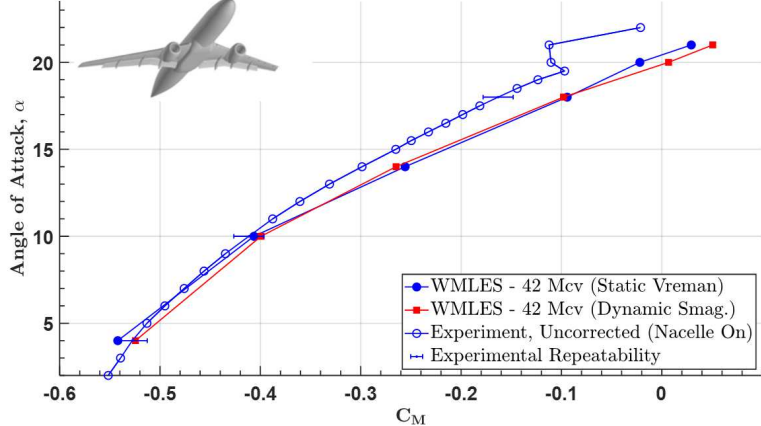


FIGURE 6. Aircraft angle of attack (α) in degrees plotted against aircraft moment coefficient (C_M) for the JAXA standard model (nacelle/pylon on configuration) as compared with the predictions of charLES using two SGS modeling approaches: static Vreman and dynamic Smagorinsky.

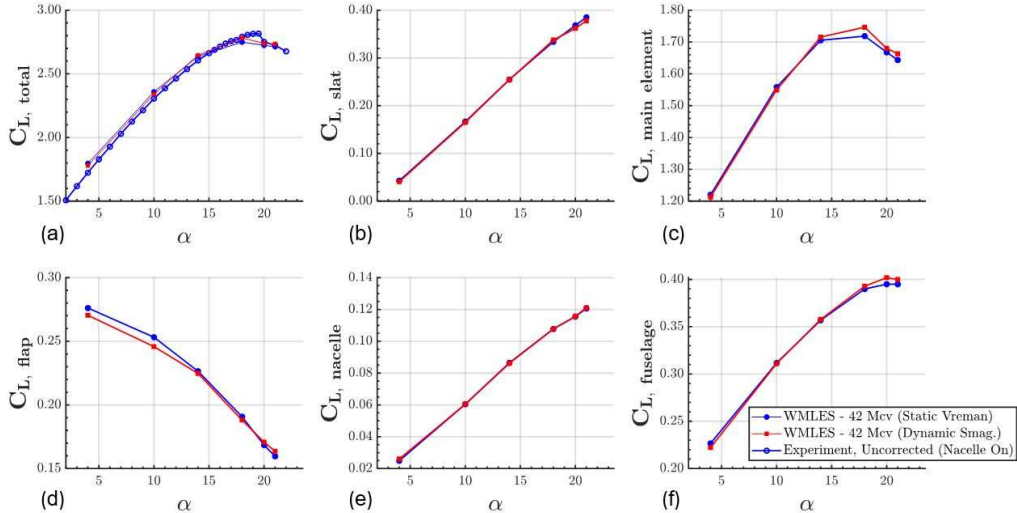


FIGURE 7. Breakdown of the total C_L (a) into contributions from various components of the aircraft, including sub-components of the wing (slat - (b), main element - (c), flap - (d)), the nacelle (e), and the fuselage (f) as predicted by charLES using two SGS modeling approaches: static Vreman and dynamic Smagorinsky across all simulated angles of attack α (in degrees).

trailing-edge flaps, which, somewhat counter intuitively, are most highly loaded when the aircraft is at a low angle of attack, and therefore most likely to separate (Chin *et al.* 1993). We investigate further by considering the sectional pressure coefficients at six spanwise stations along the wing shown in Figure 8 and find in general very good agreement between the two modeling approaches and the experimental measurements, except near the 33% semispan location, where the flap suction is over-predicted. By visualizing the average velocity contours shown in Figure 9, we can ascertain that indeed the DSM predicts lower lift than the Vreman model, at least in part due to a prediction

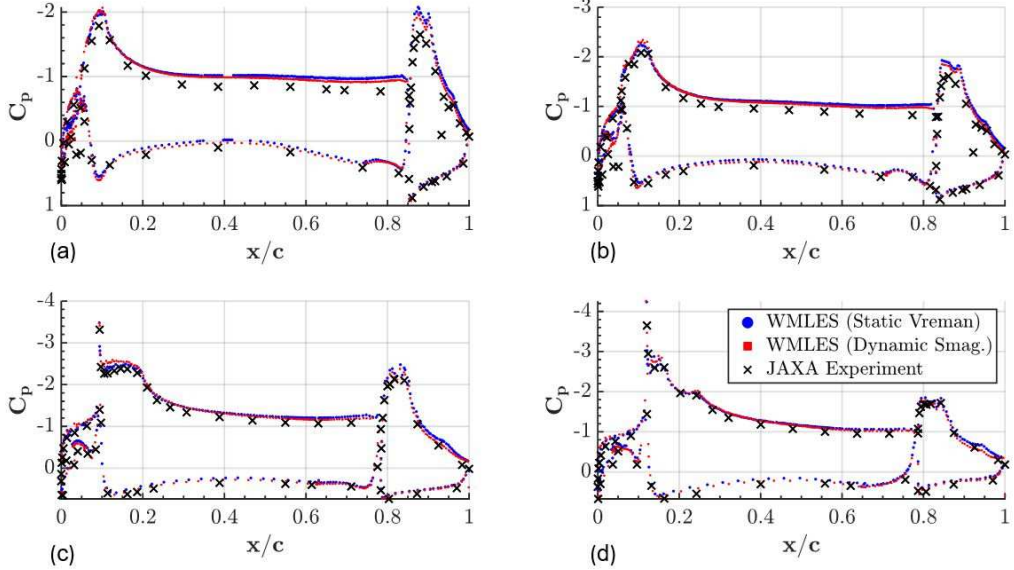


FIGURE 8. Comparison of sectional pressure coefficient, C_p , at four spanwise pressure belts (16% semispan (a), 25% semispan (b), 50% semispan (c), and 77% semispan (d)) at $\alpha = 4^\circ$ as predicted by charLES using two SGS modeling approaches: static Vreman and dynamic Smagorinsky on the same grid. Data are plotted against the local chordwise fraction, x/c . Differences are subtle, with dynamic Smagorinsky predicting less suction on the main element of the wing at the inboard stations (a,b) and improving characterization of the flow on the flap near midspan (c) and outboard (d).

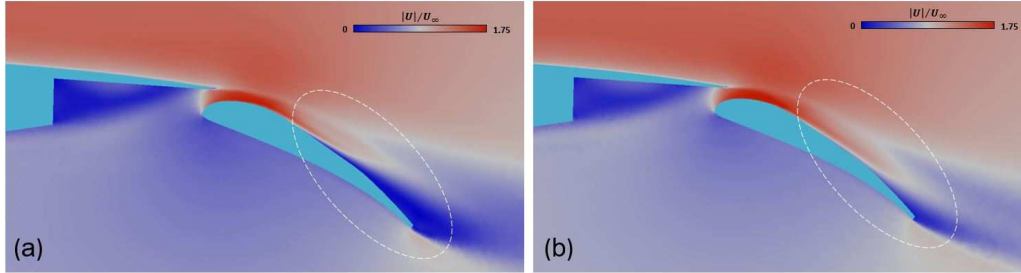


FIGURE 9. Velocity magnitude slice through the flap near the Yehudi break showing increased flap separation predicted by dynamic Smagorinsky (a) relative to static Vreman (b).

of increased flap separation, indicated in the figure by the darker colors which reflect the region of slow-moving fluid that has separated from the surface of the flap. The merging of the shear layer from the main element of the wing with the flap wake is also visible in Figure 9. This combination of evidence points to the fact that DSM outperforms static Vreman in the linear region of the lift curve due to a prediction of increased flap separation, which is consistent with the trend observed in the experimental pressure measurements, which showed less suction than our simulations.

4.1.2. Region of the lift curve near $C_{L,max}$

In this section, we seek to identify the reason behind the superior performance of DSM relative to Static Vreman in the near-stall region of the lift curve, in particular we will

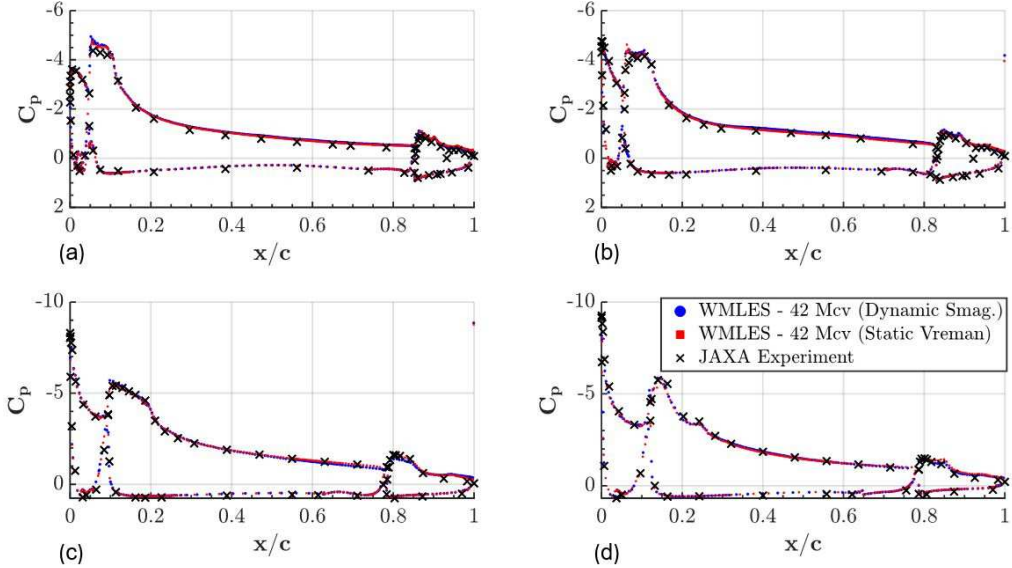


FIGURE 10. Comparison of sectional pressure coefficient, C_p at four spanwise pressure belts (16% semispan (a), 25% semispan (b), 50% semispan (c), and 77% semispan (d)) at $\alpha = 18^\circ$ as predicted by charLES using two SGS modeling approaches: static Vreman and dynamic Smagorinsky on the same grid. Data are plotted against the local chordwise fraction, x/c . Differences are not readily discernible, suggesting the improved performance of dynamic Smagorinsky near stall is accounted for by regions that are under-sampled by the experimental pressure belts.

consider the $\alpha = 18^\circ$ condition. In this case, the static Vreman model was deficient in lift relative to the experiment, as shown in Figure 4. Figure 7 shows that the main element is primarily responsible for the augmented lift that the DSM model predicts. Sectional pressure measurements in Figure 10 do not reveal glaring differences between the predictions of the two models, which suggests that the difference in lift is accounted for by a region which is not sampled by a pressure belt, such as the juncture. Since the wing area is quite large near the wing root, slight differences may integrate out into meaningful differences in C_L . Indeed, when we consider a qualitative comparison between an experimental oil-flow image and average skin friction contours in the wing/body juncture region, we find differences between the two models (Figure 11). In particular, the DSM model predicts a larger region of flow turning at the juncture, which extends almost to the first inboard pressure belt (dashed line), in contrast to static Vreman, in which the region in which the flow turns away from the juncture is very narrow. The prediction of DSM is closer to that observed in the experiment, as the region of flow turning visible in the oil flow also extends almost to the first pressure belt.

5. Results: 10 Mcv grid

A coarser grid was considered for the purpose of evaluating the sensitivity of our conclusions to grid resolution. The grid was coarsened by removing the finest layer of grid refinement at the wall in the 42 Mcv grid. Surprisingly, the solution on the coarser grid showed less sensitivity to the choice of SGS model than on the finer grid, potentially because at these resolution levels, the grid is so coarse that the input to the SGS model from the resolved LES field is too crude to expose model performance in a meaningful

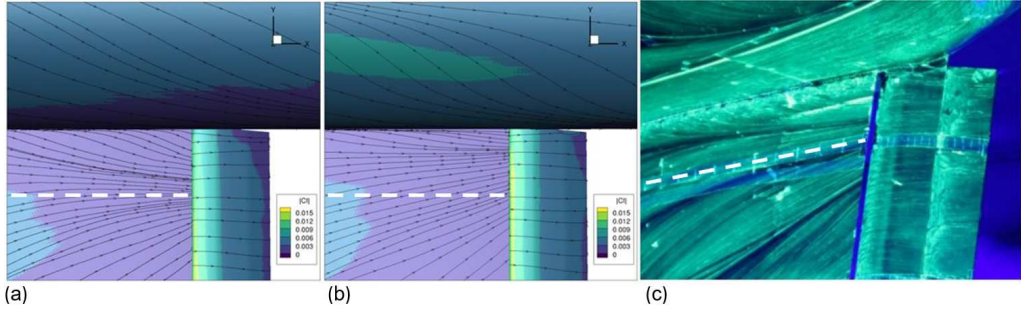


FIGURE 11. Average skin friction contours (two left graphics) from charLES predicted using two different SGS models and an experimental oil flow visualization (right) at a near-stall angle of attack ($\alpha = 18^\circ$). The dashed white line indicates the location of the first pressure belt. The Dynamic Smagorinsky model better reproduces the character of the flow at the wing/body juncture observed in the experiment than does Static Vreman.

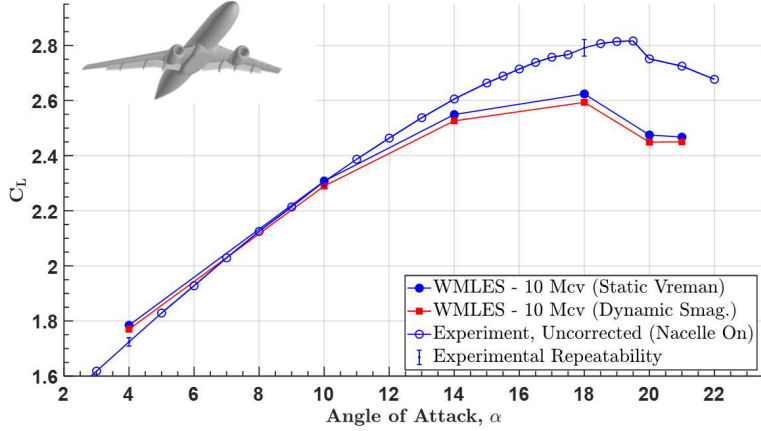


FIGURE 12. Lift coefficient (C_L) plotted against aircraft angle of attack (α) in degrees for the JAXA standard model (nacelle/pylon on configuration) as compared with the predictions of charLES using two SGS modeling approaches: static Vreman and dynamic Smagorinsky on a coarse 10 Mcv grid.

way. Figure 12 shows that the lift curves predicted by both modeling approaches are deficient in lift and nearly identical in character across the lift curve. Sectional pressure coefficients in Figure 13 reveal that the grid refinement primarily leads to an improved prediction of lift because of an improved characterization of the flow on the wingtip.

6. Conclusions

We have simulated a high-lift aircraft configuration at two resolution levels to assess the sensitivity of the prediction of integrated forces and moments to the choice of SGS model. Our two grids numbered 10 Mcv and 42 Mcv and contained approximately $\delta_{chord}/\Delta = 10$ and $\delta_{chord}/\Delta = 20$, meaning that by the trailing edge of the main element, we have between 10 and 20 points per boundary-layer thickness in all directions, since the grids contain locally isotropic cells. The simulations on a 42 Mcv grid highlight the superior performance of DSM, with the model coefficient dynamically set and varying in time and space, relative to the static coefficient Vreman model, with the model coefficient set

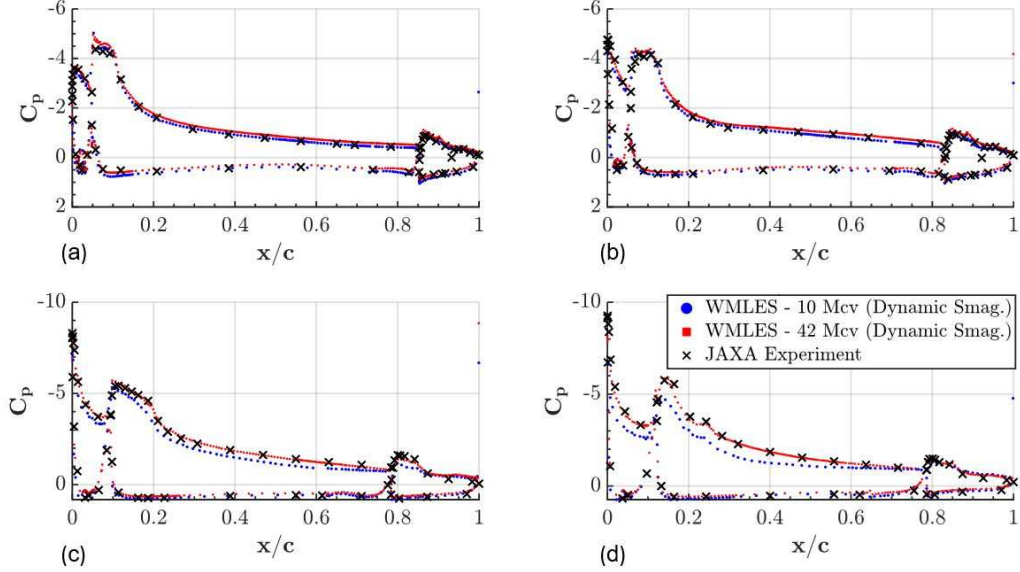


FIGURE 13. Comparison of sectional pressure coefficient, C_p , at four spanwise pressure belts (16% semispan (a), 25% semispan (b), 50% semispan (c), and 77% semispan (d)) at $\alpha = 18^\circ$ as predicted by charLES using the same SGS modeling approach, dynamic Smagorinsky, on a coarse and a refined grid. Data are plotted against the local chordwise fraction, x/c . The refined grid improves the predictions, particularly near the wingtip.

based on calibration to match the dissipation rate of homogeneous isotropic turbulence. The superiority was not limited to a particular flow phenomenon as DSM outperformed static Vreman in the characterization of both the trailing edge flap separation at low α and the wing/body juncture flow near $C_{L,max}$, suggesting it has a broader predictive scope than static Vreman. Observations of the flap and in the juncture region obtained with the DSM model were in better agreement with experimental observations. The improved predictions of DSM came with a cost increase of $\approx 15\%$ on a core-hour per flow-pass basis relative to static Vreman, owing to the computational expense of the dynamic procedure. The strict accuracy tolerances put forward by the aerospace industry (Clark *et al.* 2020) should be considered when making modeling choices in the context of flows over realistic aircraft configurations. High-fidelity SGS models with dynamically computed model coefficients provide a tractable path toward that end.

Acknowledgments

Computing resources were awarded through NASA High-End Computing (ARMD-20-8936) and research funding was provided by NASA (grant # NNX15AU93A) and Boeing Research & Technology.

REFERENCES

- BOSE, S. T. & PARK, G. I. 2018 Wall-modeled large-eddy simulation for complex turbulent flows. *Annu. Rev. Fluid Mech.* **50**, 535–561.
- CHIN, V., PETERS, D., SPAID, F. & MCGHEE, R. 1993 Flowfield measurements about a multi-element airfoil at high Reynolds numbers. *AIAA Paper 1993-3137*.
- CLARK, A. M., SLOTNICK, J. P., TAYLOR, N. J. & RUMSEY, C. L. 2020 Requirements and challenges for CFD validation within the high-lift common research model ecosystem. *AIAA Paper 2020-2772*.
- DU, Q., EMELIANENKO, M. & JU, L. 2006 Convergence of the Lloyd algorithm for computing centroidal Voronoi tessellations. *SIAM J. Numer. Anal.* **44**, 102–119.
- GERMANO, M., PIOMELLI, U., MOIN, P. & CABOT, W. H. 1991 A dynamic subgrid-scale eddy viscosity model. *Phys. of Fluids A-Fluid Dynamics* **3**, 1760–1765.
- GOC, K., BOSE, S. & MOIN, P. 2019 Wall-modeled large-eddy simulation of aircraft in landing configuration. *Annual Research Briefs*, Center for Turbulence Research, Stanford University, pp. 3–14.
- GOC, K., BOSE, S. & MOIN, P. 2020 Wall-modeled large eddy simulation of an aircraft in landing configuration. *AIAA Paper 2020-3002*.
- HAM, F., MATTSSON, K. & IACCARINO, G. 2006 Accurate and stable finite volume operators for unstructured flow solvers. *Annual Research Briefs*, Center for Turbulence Research, Stanford University, pp. 243–261.
- ITO, Y., MURAYAMA, M., YOKOKAWA, Y., YAMAMOTO, K., TANAKA, K. & HIRAI, T. 2019 Wind tunnel interference effects on Japan Aerospace Exploration Agency's Standard Model. *AIAA Paper 2019-2178*.
- LILLY, D. K. 1992 A proposed modification of the Germano subgrid-scale closure method. *Phys. Fluids A-Fluid Dynamics* **4**, 633–635.
- POINSOT, T. J. & LELE, S. 1992 Boundary conditions for direct simulations of compressible viscous flows. *J. Comput. Physics* **101**, 104–129.
- RUMSEY, C. L., SLOTNICK, J. P. & SCLAFANI, A. J. 2018 Overview and summary of the Third AIAA High Lift Prediction Workshop. *AIAA Paper 2018-1258*.
- VREMAN, A. 2004 An eddy-viscosity subgrid-scale model for turbulent shear flow: Algebraic theory and applications. *Phys. fluids* **16**, 3670–3681.
- YOKOKAWA, Y., MURAYAMA, M., KANAZAKI, M., MUROTA, K., ITO, T. & YAMAMOTO, K. 2008 Investigation and improvement of high-lift aerodynamic performances in low-speed wind tunnel testing. *AIAA Paper 2008-350*.